Class	Embedding-based			Reconstruction-based			
	Spade [6]	PaDiM [8]	CFlow [13]	DRAEM[40]	UniAD [36]	Ours	Ours*
bottle	(98.4, 95.5)	(98.5, 95.3)	(99.0, 96.8)	(99.1, **97.2**)	(98.0, 93.8)	(97.7,95.0)	(97.7,95.0)
cable	(97.2, 90.9)	(98.1, 91.1)	(97.7, 93.5)	(94.7, 76.0)	(97.2, 86.3)	(95.2,88.7)	(95.6,**89.5**)
capsule	(99.0, 93.7)	(98.8, 92.3)	(99.0, 93.4)	(94.3, **91.7**)	(98.7, 90.8)	(98.0,90.1)	(97.5,91.4)
carpet	(97.5, 94.7)	(98.9, 94.5)	(99.3, 97.7)	(95.5, 92.9)	(98.4, 94.5)	(98.9,95.8)	(98.9,**95.8**)
grid	(93.7, 86.7)	(96.1, 90.5)	(99.0, 96.1)	(99.7, 98.4)	(97.5, 92.6)	(99.1,98.1)	(99.1,**98.4**)
hazelnut	(99.1, 95.4)	(98.4, 84.0)	(98.9, 96.7)	(99.7, **98.1**)	(98.2, 93.0)	(97.7,89.5)	(97.3,91.1)
leather	(97.6, 97.2)	(99.2, 97.9)	(99.7, 99.4)	(98.6, 98.0)	(98.7, 97.2)	(99.5,99.1)	(99.5,**99.1**)
metal nut	(98.1, 94.4)	(98.0, 92.9)	(98.6, 91.7)	(99.5, **94.1**)	(94.9, 87.1)	(96.8,93.0)	(96.8,93.0)
pill	(96.5, 94.6)	(97.0, 95.3)	(99.0, 95.4)	(97.6, 88.9)	(96.2, **95.3**)	(92.5,94.5)	(92.5,94.5)
screw	(98.9, 96.0)	(98.7, 94.6)	(98.9, 95.3)	(97.6, **98.2**)	(98.9, 95.3)	(99.0,95.6)	(99.0,95.6)
tile	(87.4, 75.9)	(94.3, 93.7)	(98.0, 94.3)	(99.2, **98.9**)	(92.0, 79.6)	(92.1,95.1)	(92.1,95.1)
toothbrush	(97.9, 93.5)	(98.7, 94.3)	(98.9, 95.1)	(98.1, 90.3)	(98.3, 88.2)	(98.9,94.7)	(98.6,**95.7**)
transistor	(94.1, 87.4)	(97.9, 91.4)	(98.0, 81.4)	(90.9, 81.6)	(97.9, **93.9**)	(92.6,89.7)	(93.1,90.1)
wood	(88.5, 87.4)	(95.7, 89.3)	(96.7, 95.8)	(96.4, **94.6**)	(93.0, 86.0)	(94.7,92.9)	(94.5,93.0)
zipper	(96.5, 92.6)	(98.5, 95.0)	(99.0, 96.6)	(98.8, **96.3**)	(97.7, 93.2)	(97.6,93.6)	(97.6,93.6)
average	(96.0, 91.7)	(97.8, 92.8)	(98.6, 94.6)	(97.3,93.0)	(97.0, 91.1)	(96.7,93.7)	(96.7,**94.1**)

Table 1: Compare with the state-of-the-art anomaly detection approaches on MVTec-AD [3] dataset. We compare anomaly localization performance with pixel-wise AUROC and PRO metrics, denoted as (AUROC, PRO) in the table. We highlight the best PRO scores among all the reconstruction-based methods. We denote the result in Red if the result underperforms other reconstruction-based methods by a large margin. We show our results with the same hyperparameters for all categories, denoted as Ours, and different hyperparameters adjusted for each category, denoted as Ours*.

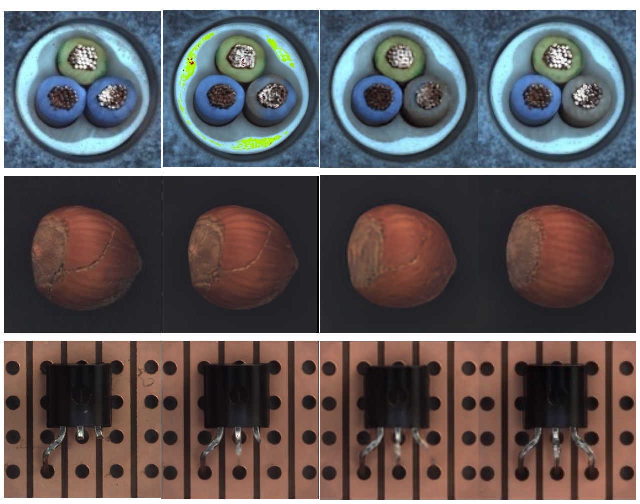

(a) Input (b) DRAEM (c) UniAD (d) Ours

Figure 4: Comparisons of the reconstruction results on class cable and hazelnut of MVTec-AD. The anomaly types are color-swap, crack, and cut-lead for the three categories.

represent ground truth, our pixel-level anomaly predictions, our feature-level anomaly predictions, and the final results visualized on the original images. We show that our denoising model is capable of precise boundary estimation of anomalies.

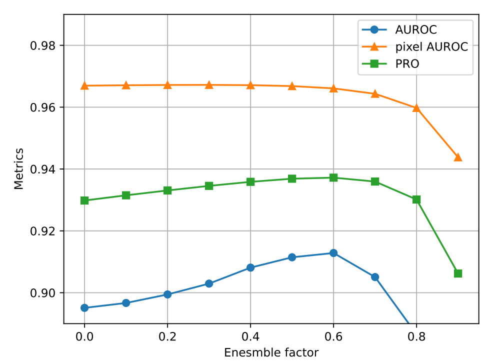

Figure 5: The effects of different ensembling factor α.

4.4. Ablation study

Ensemble factor. We combine the pixel-level and feature-level 11 predictions to get the final anomaly score. We conduct experiments to verify the effects of the ensembling weights. As Fig. 5 shows, we choose the best ensemble factor $\alpha = 0.5$. The PRO metric is improved by 0.7% compared with only using the feature-level anomaly score.

Pretrained feature extractor. We observe that the deep features extracted by ResNet [14] and WideResNet [39] are of high dimensional, which brings great difficulties for our denoising model to reconstruct the features. Instead, we